Dynamics of a high-eccentricity planet in a large planetesimal disc

Martin Montelius

Lund Observatory
Lund University

2019-EXA153

Degree project of 15 higher education credits
June 2019

Supervisor: Alexander Mustill

Lund Observatory
Box 43
SE-221 00 Lund
Sweden

Abstract

Clustering of orbital characteristics for distant Solar System objects has been proposed to indicate the presence of a ninth planet. Simulations show that the planets orbit would have to have a mass of $5-10M_{\oplus}$, a semi-major axis of $400-800$ AU, an eccentricity of $0.2-0.5$ and an inclination of $15^{\circ}-25^{\circ}$. Simulations of a planet scattering off a giant planet into an highly eccentric orbit, show that the scattered planet can circularise its orbit by dynamical friction with a planetesimal disc, providing a hypothesis of the origins of Planet Nine. The simulations show an increase in the planets inclination not explained by dynamical friction.

In this thesis a further examination of the increasing inclination is presented. Some of the theory of the Kozai–Lidov resonance, phase space, dynamical friction and the Miyamoto–Nagai potential is presented. The results show that a highly eccentric planet travelling through a planetesimal disc is reliably circularised and achieves high inclination at some point of its evolution. The phase space for the Kozai–Lidov resonance for this setup is explored. Additional fixed points at 0 and 180 degrees, which are not present in the regular Kozai cycle, are found to play a major role in the dynamics as the planet is circularised.

An attempt was made to model the planetesimal disc with the Miyamoto–Nagai potential. Simulations were performed for different values of the disc parameters. The resulting phase portraits lacked the additional fixed points produced by the planetesimal disc.

Populärvetenskaplig beskrivning

Ända sedan 1781, när William Herschel upptäckte Uranus, så har astronomer letat efter planeter som ligger ännu längre ut. Solsystemet är ett stort ställe, så om man vill hitta någonting så krävs lite vägledning till var man ska leta. 2016 publicerade astronomerna Konstantin Batygin och Mike Brown en studie om små objekt utanför Neptunus, där de hade upptäckt att många av de här himlakropparnas banor delar vissa egenskaper. De föreslog att det här orsakas av en oupptäckt planet, kallad Planet Nio, på en utdragen omloppsbana långt ifrån de planeterna vi redan känner till.

Ett problem med den här hypotesen är att vi inte vet hur Planet Nio skulle ha hamnat så långt bort. Om den bildades där ute så förklarar det inte hur den omloppsbana blev så utdragen. I andra teorier föreslås det att den bildades någon annanstans. Solen hade kunnat ta planeten från en annan stjärna som passerat för nära, eller så kunde Planet Nio ha bildats med de andra planeterna och blivit utslungad av något nära möte. Om den senare teorin stämmer så skulle det förklara varför banan är så utdragen, det är vanligt för objekt som har slungats ut bortom de andra planeterna. Men det finns ett problem med teorin, den har svårt att förklara varför den förslagna banan lutar så mycket jämfört med de andra planeterna.

2018 föreslog Linn Eriksson vid Lunds Universitet en ny ide för hur planetens bana hade kunnat utvecklas, från att den slungats ut, tills att den är på den bana som forskarna tror at den har. I hennes modell så interagerar planeten med ett asteroidbälte som inte har upptäckts än. Projektet var mest fokuserat på hur excentrisk banan skulle bli, men mot förmodan så fick planetens bana en lutning som matchar förutsägelserna som gjorts. Det här kandidatarbetets fokus har legat på att förstå varför banan fick lutningen och hur planeten och bältet interagerar.

Det här arbetet kan vara användbart för astronomer i flera områden. Med en förbättrad förståelse för hur Planet Nio bildats så ökar våra chanser att en dag hitta den. Om teorin stämmer så skulle den kunna stödja olika teorier om planetbildning. Även om vi inte hittar Planet Nio så skulle arbetet kunna användas för att bättre förstå hur planeter runt andra stjärnor beter sig, eftersom många av dem har banor som likar banan som föreslagits för Planet Nio.

Acknowledgements

I would like to give a heartfelt thanks to my supervisor, Dr. Alexander James Mustill, who guided me through all the twists and turns this project presented. At the beginning of the project I was a novice in many of the fields we have explored, and unfamiliar with the software I needed to use. The encouragement I received to learn new things has been invaluable and I will always carry it with me.

I would also like to thank the other Bachelor students whom I worked together with in the library, my code would never be the same without you.

Finally, thank you to my friends and family who have let me explain my thesis for them, the questions and comments have been essential for my understanding.

Contents

List of Figures

List of Tables

Chapter 1

Introduction

Since Neptune was discovered in 1846 by investigating anomalies in Uranus' orbit, astronomers have searched for more distant planets by studying the orbits of the other bodies in the Solar System. Current research focuses on ETNOs, Extreme Trans-Neptunian Objects, and what appears to be a clustering in both physical space and in some of their orbital features (Trujillo and Sheppard 2014; Batygin and Brown 2016). It is believed that the clustering can be explained by an as of yet undiscovered object, dubbed Planet Nine. Simulations show favourable results for a Planet Nine with a mass between 5 - 10 $M_\oplus$ in an orbit with a semi-major axis of 400 - 800 AU, an eccentricity between 0.2 and 0.5 and an inclination of 15 - 25° (Brown 2019).

This proposed orbit is markedly different from the other Solar System planets orbits. An explanation is needed for where the planet was formed and how it was put on its current orbit. The three main theories are *in-situ* formation (Kenyon and Bromley 2016), a capture event (Mustill, Raymond, and Davies 2016) or a scattering event. The scattering event theory proposes that Planet Nine was formed in the giant planet region of the Solar System and due to a close encounter with another giant planet it was scattered onto a highly eccentric orbit. This initial configuration of a five giant planet Solar System has been shown to produce results for the evolution of the Solar System which are equally as valid as those produced with four giant planets (Batygin, Brown, and Betts 2012). An initial fifth giant planet could also help explain certain orbital features of the other giant planets (Nesvorný and Morbidelli 2012). To avoid subsequent scatterings, and possible ejection from the Solar System, some gravitational interaction is required to circularise the orbit. The first proposed mechanism for this purpose was fly-by encounters with other stars. The problem with this proposal is that Planet Nine is successfully circularised onto an orbit which can explain the observed clustering in $\leqslant 5\%$ of simulations (Li and Adams 2016).

In Eriksson et. al. (2018) a new proposal for how Planet Nine could be circularised is presented. The perturber in this model is a massive belt of planetesimals beyond 100 AU, referred to in the paper as a cryobelt. The existence of such a belt is as yet hypothetical. However, its existence is consistent with Carrera et. al. (2017), in which simulations of planetesimal formation by the streaming instability with far ultra violet photoevapo-

ration predicts that at least $60M_{\oplus}$ of planetesimals will form beyond 100 AU. Further improvements to the model, accounting for different fragmentation speed, turbulence and disc parameters, showed even greater masses of planetesimals formed (Carrera et al. 2017). The rate of successful circularisations with the model presented in Eriksson et. al. (2018) is $20 - 30\%$.

If the only interaction between Planet Nine and the cryobelt is dynamical friction, it would be expected that both eccentricity and inclination would be dampened. As the planet's inclination in Eriksson et. al.'s simulations is increasing, another mechanism must be involved. Eriksson et. al. proposes that this mechanism is the Kozai–Lidov resonance, as while the planets' inclination is increasing, its argument of periapsis oscillates around a fixed value.

The aim of this thesis project is to investigate the nature of the mechanism causing the deviations from the expected result of Eriksson et. al.'s model. To achieve this goal, firstly the relevant parts of their simulations will be replicated. Secondly, the system will be studied in a frictionless setup to better understand the impact of dynamical friction.

Chapter 2

Theory

2.1 Keplerian orbital elements

The six degrees of freedom required to give the position and velocity of an object can be expressed in a number of ways. When performing N-body simulations Cartesian position and velocities are useful, but they are less helpful when attempting to visualise an orbit. For that purpose Keplerian orbital elements, illustrated in figure 2.1, are often used. Kepler's first law states that all planetary orbits are ellipses with the Sun at one of the focal points. The semi-major axis, a_{pl}, and the eccentricity, e, define the size and shape of the ellipse as

$$e = \sqrt{1 - \frac{b_{pl}^2}{a_{pl}^2}}, \tag{2.1}$$

where b_{pl} is the orbits semi-minor axis. The orbit's angle to some reference plane is set by the inclination, i. The orbit's orientation to that reference plane is fixed by two elements: the argument of periapsis, ω, which is the angle between the ascending node, where the orbit intersects with the reference plane in the direction of motion and the line of apses, where the body makes its closest approach to the Sun; and the longitude of the ascending node, Ω, which is the angle in the reference plane between the ascending node and a reference direction, in the Solar System this is usually the vernal equinox. The final element is the true anomaly, ν. It determines the position of the planet at a given time with the angle between the line of apses and the planet's radius vector in the orbital plane. In a two body system only the true anomaly will change. This is in contrast to Cartesian coordinates which always varies over an orbit. If the orbit is perturbed and the value of one or more of the elements change, information about the nature of what perturbed the orbit can be obtained by studying the time evolution of the orbital elements.

2.2 Kozai–Lidov resonance

The following discussion about the Kozai–Lidov resonance and the following section 2.3 on dynamical friction are based on the derivations in *The three-body problem* (Valtonen and

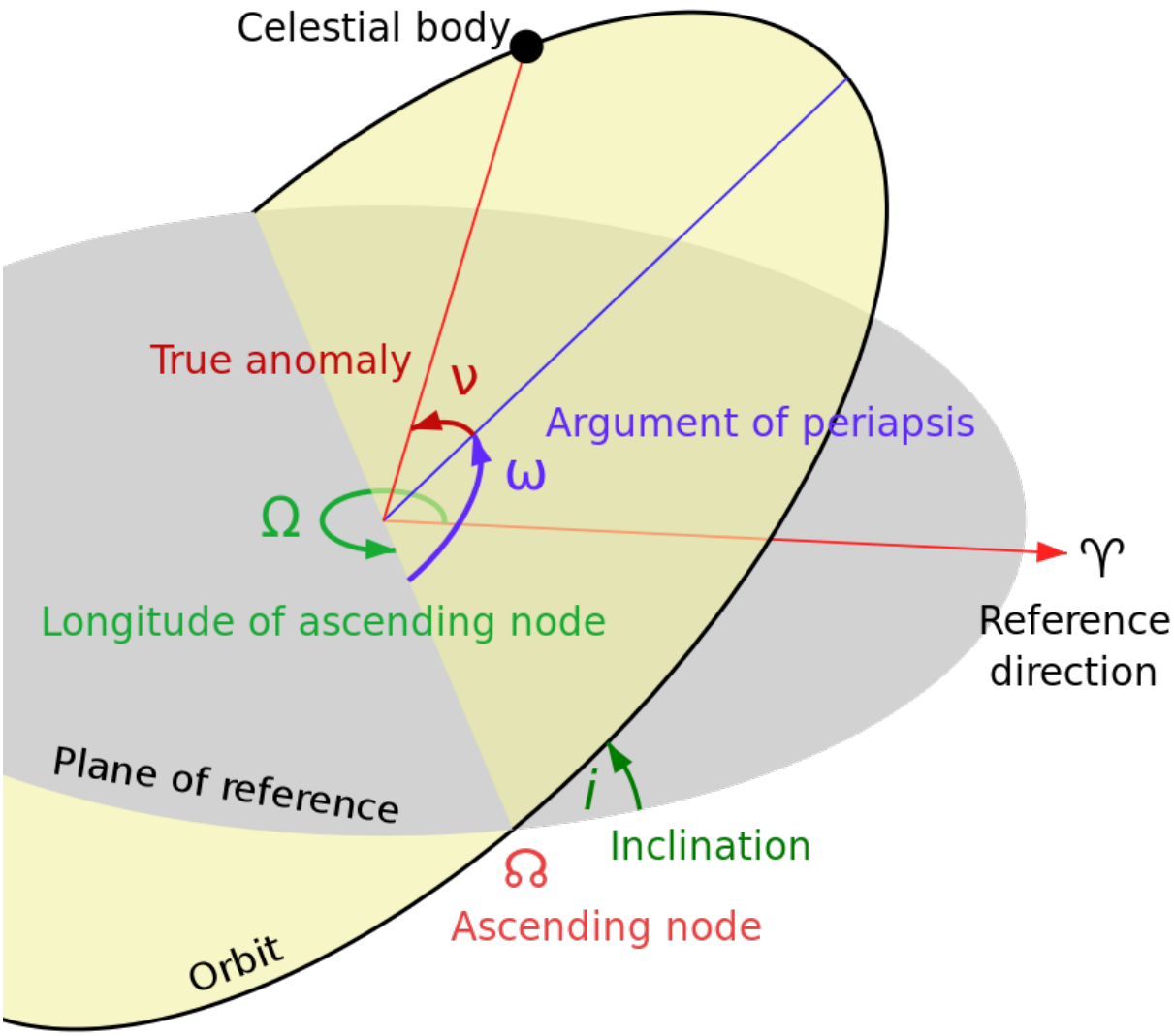

Figure 2.1: Illustration of some of the Keplerian orbital elements and the reference plane and direction which are used to define them. Image from (Wikipedia, the free encyclopedia 2007)

.

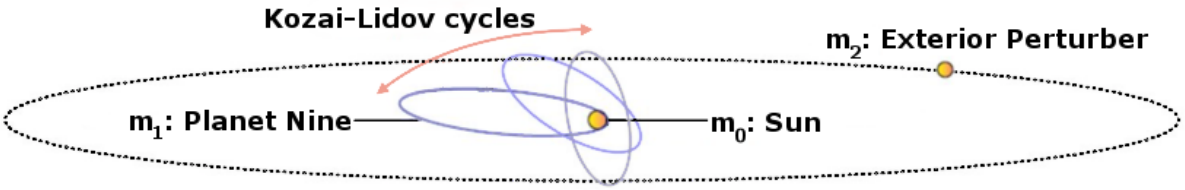

Figure 2.2: Illustration of a setup which will produce a classical Kozai cycle, note that this is not the setup which is considered in this thesis. Image source: (Batygin, 2018; edited)

Karttunen 2006).

One kind of system in which the Keplerian orbital elements are perturbed, is the hierarchical three body system. In this system two bodies, m_0 and m_1, orbit each other in a binary and are perturbed by a distant third body, m_2. m_0 is assumed to be significantly more massive than the other bodies, and m_1 is assumed to have a negligible mass compared to m_2. An example of such a setup is seen in figure 2.2, where the Sun is m_0, Planet Nine is m_1 and m_2 is some unknown exterior perturber.

The perturbation will cause m_1 to enter into a resonance, where the argument of periapsis will oscillate around a fixed value, meaning that the rate of precession for the pericenter and the line of nodes is equal. The resonance was described separately in 1961, by Mikhail Lidov during the study of man-made satellites being affected by the Moon, and in 1962, by Yoshihide Kozai studying asteroids being affected by Jupiter (Lidov 1962; Kozai 1962). Therefore it is called the Kozai–Lidov resonance.

To describe the change in the Keplerian orbital elements caused by the perturbations of a distant perturber, Hamiltonian mechanics is used. The Hamiltonian for m_1 is divided into two parts; one for the orbital motion in the binary, and one for the perturbation from m_2. By averaging the effect of the perturbation over the orbits of m_1 and m_2 the secular evolution of m_1 can be studied. Under these circumstances it is assumed that the energy of both bodies are conserved separately, implying that their semi-major axis will be conserved. The interaction they have in the resonance is instead an exchange of angular momentum. The axial symmetry of the system will conserve the z-component of angular momentum, L_z, for m_1 and m_2. A rescaling of the conserved L_z can be expressed in terms of the eccentricity, e, and the inclination, i, of m_1,

$$c = \sqrt{1 - e^2}\cos \imath. \tag{2.2}$$

c will be referred to as the Kozai parameter in this text. It will be a constant for the case of an interior test particle with a perturber on a circular orbit.

The time derivatives of the Keplerian orbital elements can be derived from the Hamiltonian of the system,

$$
\begin{aligned}
\dot{\imath} &= -\frac{15}{8}\frac{e^2}{\sqrt{1-e^2}}\sin 2\omega \sin \imath \cos \imath \frac{A}{n}, \\
\dot{e} &= \frac{15}{8} e\sqrt{1-e^2}\sin 2\omega \sin \imath^2 \frac{A}{n}, \\
\dot{\omega} &= \frac{3}{4}\frac{1}{\sqrt{1-e^2}}\left[2(1-e^2) + 5\sin \omega^2 (e^2 - \sin \imath^2)\right]\frac{A}{n}, \\
\dot{\Omega} &= -\frac{\cos \imath}{4\sqrt{1-e^2}}(3 + 12e^2 - 15e^2 \cos \omega^2)\frac{A}{n},
\end{aligned}
\tag{2.3}
$$

with the factor $A = \frac{Gm_1m_2m_3}{m_B a_e^3 (1-e_e^2)^{3/2}}$.

2.2.1 Phase space and portraits

To visualise the time derivatives in equation 2.3 the argument of periapsis - eccentricity phase space is used. The following description of phase space draws from Goldstein et. al. (2014) with some modified terminology.

In Hamiltonian mechanics a particle is described by two sets of independent coordinates, most commonly position q and momentum p. For a conservative system where the Hamiltonian has a constant value E, the momentum can be written as a function of q and E. By plotting this function in a $p-q$ graph the possible trajectories of the function can be analysed. This representation is called phase space. Displaying different initial conditions as separate trajectories in the same plot creates a phase portrait.

There are two main types of periodic motion in phase space, libration and circulation. A librating trajectory will be a closed loop, with a bounded set of possible values. A classic example of a librating system would be a harmonic oscillator, which will oscillate around a minima of the systems kinetic energy. The distance from the minima will be bounded by the total energy of the system and can not increase indefinitely. A circulating trajectory will instead represent rotation, a continual increase in the positions value. An example would be a rigid rotating body, where the position coordinate q represents the angle of rotation. Although the function for p will be periodic in increments of 2π, the range of values q will not be bounded.

In figure 2.3 the phase portrait for a simple pendulum is shown. Orbit 1 is an example of a librating orbit and orbit 3 is an example of a circulating one. At the centre of orbit 1 is a fixed point, that is to say, a point where the time derivatives of both p and q are zero. A fixed point with librating trajectories around it is called a centre. A second centre is seen where the pendulum has turned by 2π. Between the two centres, at π, is a saddle; this is an unstable equilibrium, representing the pendulum pointing directly opposite to the direction of gravity. For the simple pendulum there must be a saddle between two centres. The area of phase space with librating trajectories around a fixed point is commonly referred to as an island.

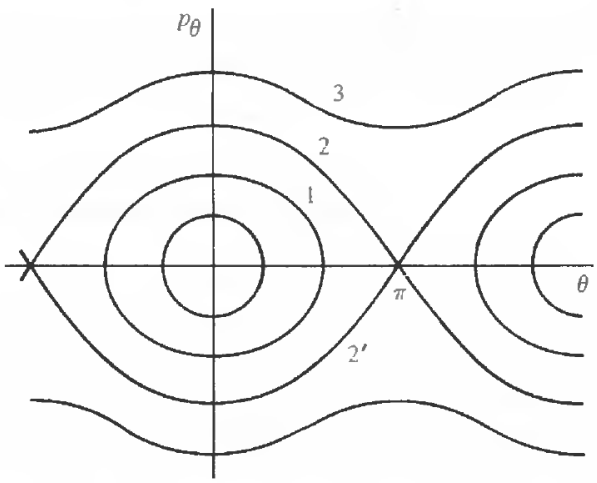

Figure 2.3: Illustration of the two kinds of periodic motion and fixed points which are found in the phase portrait for the Kozai cycle (Goldstein, Poole, and Safko 2014, fig 10.3)

.

Phase portraits can be constructed for other coordinate pairs than position and momentum. As the Kozai parameter represents a conserved quantity we can find fixed points for this system as well.

Finding a solution for $\dot{e} = 0$ gives the conditions for having a fixed point in the evolution of the planet's orbit. A trivial solution exists for when the eccentricity or the inclination is zero. The other solutions require ω to be a multiple of 90°. $\dot{\omega}$ being zero tightens the requirement to 90° and 270°, giving us our fixed points in the $\omega - e$ phase space.

Around these fixed points, the conservation of the Kozai parameter causes an exchange of eccentricity and inclination. Creating a phase portrait for the $\omega - e$ phase space illustrates the change in eccentricity. The properties of the phase space will be determined by the value of the Kozai parameter. To illustrate this I have performed simulations of planets orbiting at 600 AU with periodically varied values of eccentricity and argument of periapsis, which are being being perturbed by a massive planet at 1500 AU, a setup closely resembling the one in figure 2.2. The simulations were made with the program MERCURY6, described in section 3.1. The phase portraits produced are seen in figure 2.4. The trajectories for the planets which librate have been highlighted in red, while the circulating trajectories are displayed in black. For a falling value of the Kozai parameter the location of the fixed points will fall, until they reach a critical value at $c \approx 0.77$ (Valtonen and Karttunen 2006) and vanish. This occurs at this specific value because of the differential equations in equation 2.3. For an eccentricity going to 0, $\dot{\omega} = 0$ will only hold for $i = 39.23°$, meaning that there are no fixed points for lower inclinations and higher values of the Kozai parameter. To uniquely determine e and i the value of e cannot exceed a certain threshold, set by the Kozai parameter. At $c = 1$ all eccentricities are uniformly 0, or alternatively all the inclinations are 90°.

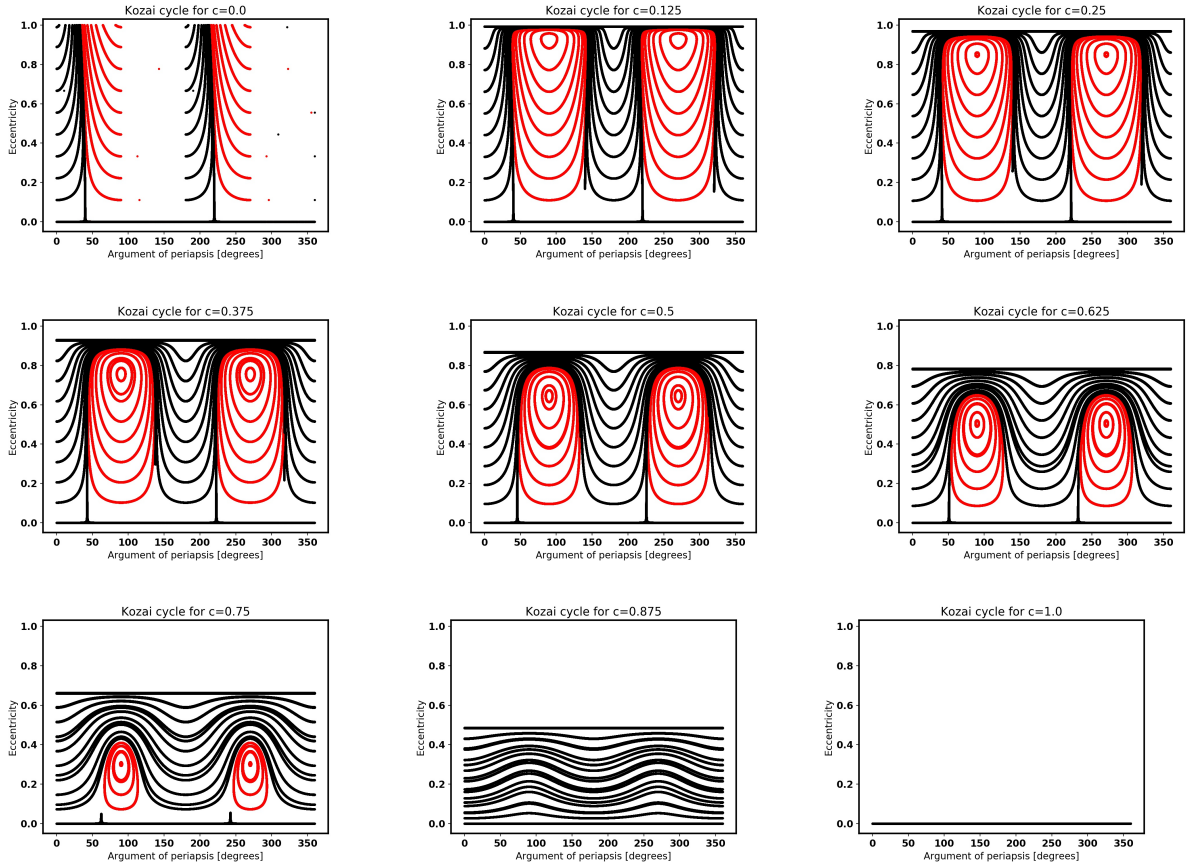

Figure 2.4: Illustration of what a regular Kozai cycle with a distant perturber looks like at different values of the Kozai parameter in equation 2.2. The black trajectories are circulating and the red ones are librating.

2.3 Dynamical friction

The second mechanism which is important for this thesis is dynamical friction. While moving through a medium of comparatively light bodies, a heavy body will experience a number of hyperbolic two-body encounters. The gravity of the larger body will accelerate the smaller body, and cause the larger body to lose some orbital energy after the encounter. Assuming a homogeneous medium, the contributions to the velocity perpendicular to the direction of motion will cancel each other out. Depending on the density of the medium and the mass and velocity of the body, the velocity of the body will decrease.

It is expected that dynamical friction will dampen the eccentricity and inclination of the bodies moving through the medium (Kokubo and Ida 1995; Del Popolo, Spedicato, and Gambera 1999). In the context of the Kozai resonance described in section 2.2, this dampening will have a two-fold effect, directly dampening the eccentricity, and changing the Kozai parameter. To illustrate these two effects figure 2.5 shows two possible outcomes

for an initial trajectory with $c = 0.50$, seen in blue:

- The image to the right shows the first scenario, where the dampening of eccentricity is more important than the change in the Kozai parameter. This allows the trajectory to traverse the phase portrait, possibly changing from circulating to librating, as seen with the red trajectory, or *vice versa*.
- The image to the right shows the other scenario, where the change in the Kozai parameter is the more significant process. In this case the phase portrait has changed, the fixed points have sunk to lower eccentricities. Because of this, the red trajectory follows a different path than the blue trajectory, despite both trajectories starting at similar eccentricities at $\omega = 0$.

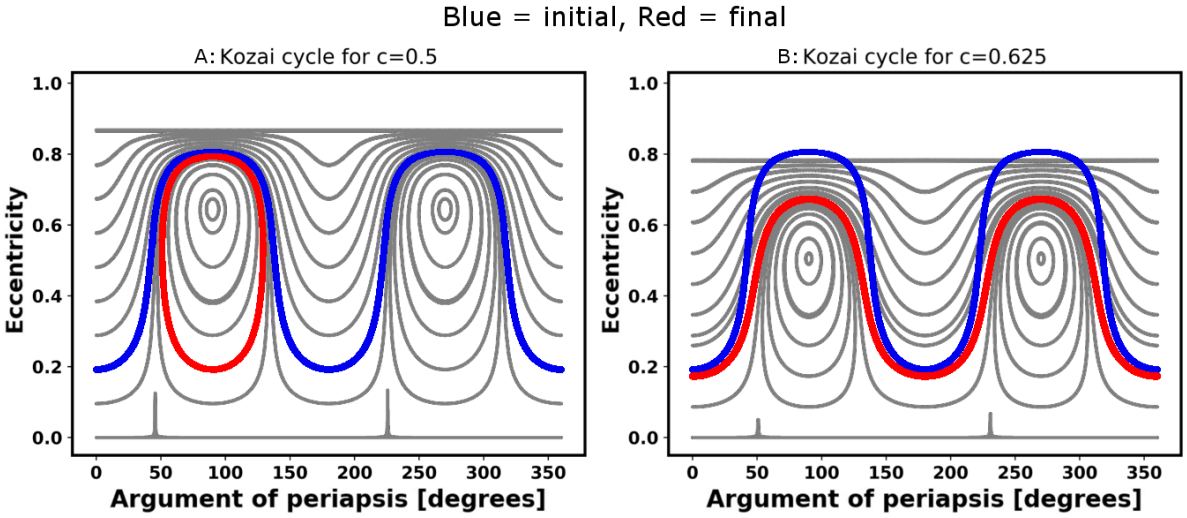

Figure 2.5: Illustration of the competing effects of eccentricity being dampened. The blue line shows an initial circulating trajectory for $c = 0.50$. The image to the left shows a librating trajectory in red, illustrating a possible outcome of the eccentricity dampening being a more significant effect than the change in the Kozai parameter. The image to the left displays a circulating trajectory for $c = 0.625$ in red, a possible outcome of the Kozai parameter changing while the eccentricity is only mildly affected.

2.4 Disk potential

As N-body simulations will eventually be limited by the scaling factor between the number of bodies and the time it takes to run the simulation, large systems often use some other method to mimic the bodies with something less computationally intensive. The Miyamoto–Nagai potential was constructed for such a purpose, to simulate the mass distribution of disc galaxies (Miyamoto and Nagai 1975). The potential corresponds to a

radially symmetric disk described by two characteristic lengths representing thickness, b, and radius, a. After these cutoff points the potential will decrease proportionally to R^{-1}.

$$\Phi(R,z) = -\frac{GM}{\sqrt{R^2 + (a + \sqrt{z^2+b^2})^2}}. \tag{2.4}$$

The potential was chosen because of its analytical volume density formula,

$$\rho(R,z) = \frac{b^2 M}{4\pi} \frac{aR^2 + \left(a + 3\sqrt{z^2+b^2}\right)\left(a + \sqrt{z^2+b^2}\right)^2}{\left[R^2 + \left(a + \sqrt{z^2+b^2}\right)^2\right]^{5/2} (z^2+b^2)^{3/2}} \tag{2.5}$$

This volume density formula could allow the potential to be combined with the equations for dynamical friction, which require such a density.

When $b = 0$ the potential is reduced to the Kuzmin potential (Binney and Tremaine 2008), which has a well defined surface density. It is calculated as,

$$\Sigma(R) = \frac{aM}{2\pi(R^2+a^2)^{3/2}}. \tag{2.6}$$

The surface density is constant within the bounds of a, and drops of as R^{-3} after that point.

The force exerted on an object by this potential is calculated as $F = -\nabla\Phi$,

$$\begin{aligned}
F_x &= -\frac{GMx}{\left(x^2 + y^2 + \left(a + \sqrt{z^2+b^2}\right)^2\right)^{3/2}}, \\
F_y &= -\frac{GMy}{\left(x^2 + y^2 + \left(a + \sqrt{z^2+b^2}\right)^2\right)^{3/2}}, \\
F_z &= -\frac{GMz\left(a + \sqrt{z^2+b^2}\right)}{\sqrt{z^2+b^2}\left(x^2 + y^2 + \left(a + \sqrt{z^2+b^2}\right)^2\right)^{3/2}}.
\end{aligned} \tag{2.7}$$

Chapter 3

Method

The illustration in figure 3.1 shows the basic setup used as the initial conditions for this thesis. Planet Nine has just been scattered in the giant planet region into an highly eccentric orbit, which retains its pericenter distance at roughly 30 AU. The orbit crosses a large belt of planetesimals, extending from $100 - 600$ AU. The other planets in the Solar System are not included to reduce the complexity of the system.

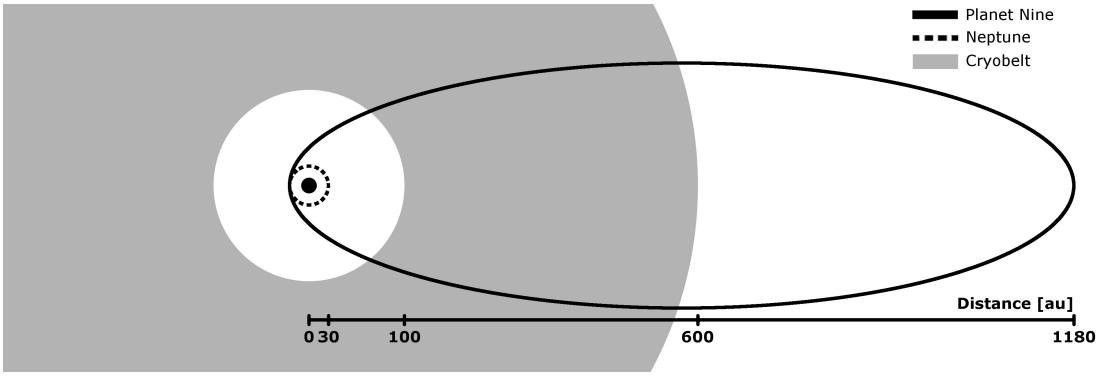

Figure 3.1: The setup for the studied system: the central point represents the Sun; the dashed line is the orbit of Neptune; the solid line is the orbit of Planet Nine; and the grey area represents the cryobelt.

Analytic solutions of problems increase in complexity with the number of bodies. Already at three bodies, full analytical solutions are only available for special cases. Studying a disc of potentially thousands of particles will therefore require numerical simulations.

Three sets of simulations were carried out during the project:

- dynamical friction simulations, with a massive planet and a massive cryobelt
- frictionless simulations, with a reduced planet mass and a massive belt, to find the shape of the phase portrait empirically
- simulations with the Miyamoto–Nagai potential, where the planet's mass was set to zero and the cryobelt was mimicked by the potential discussed in section 2.4

The Miyamoto–Nagai phase portraits were created to reduce the long computational times for the frictionless dynamics simulations and to rectify unphysical effects from close encounters between the planet and the belt particles.

3.1 The Mercury6 N-body integrator

The N-body integrator MERCURY6 (Chambers 1999) is used to carry out the simulations in this project.

A useful feature in MERCURY6 is its distinction between two kinds of input, big and small bodies. Big bodies will gravitationally interact with all the bodies in the system, while small bodies will only interact with big bodies. This greatly reduces the complexity of N-body problems, as the computational time for big bodies will scale as N^2, but only as N for small bodies.

MERCURY6 has different algorithms for solving N-body problems. In this case, the handling of close encounters and highly eccentric orbits is essential, so the Bulirsch-Stoer integrator was chosen. This algorithm works by combining different mathematical methods to solve differential equations, the following explanation of those methods largely follows that in Press et. al. (2007). The main idea of the algorithm is to take a large stepsize when evaluating the differential equations and gradually subdivide it into smaller substeps. A rational function dependent on the stepsize is fitted to the result of taking these substeps, and is evaluated for a stepsize of zero to get an approximation of what the solution would be for an infinitely small stepsize. The advantage of fitting a rational function over a polynomial one is that it remains effective even at large stepsizes. The main advantage of the Bulirsch–Stoer algorithm itself is its accuracy. The error function from evaluating the substeps will only contain even powers of the stepsize when expressed as a power series. Because of this two orders of terms can be eliminated when combining steps. This allows the Bulirsch–Stoer algorithm to be accurate to the fourth order while only solving one differential equation.

3.2 Dynamical friction simulations

For the first set of simulations a massive planet interacts with a massive belt of planetesimals to investigate the effects of dynamical friction on the planet.

Replicating a system similar to the one in Eriksson et. al. (2018), the cryobelt is modelled as MERCURY6's small bodies with near circular orbits with eccentricities below 0.01 and inclinations below 5°. The semi-major axis are set between the inner edge of the belt at 100 AU and the outer edge at 600 AU. The other orbital elements are randomised between 0° and 360° to get an axially symmetric disc. Two different surface density distributions, Σ, are used. They are distinguished by how they scale with the semi-major axis, $\Sigma^{-(\alpha=1)}$ will drop of as $\frac{1}{a_{pl}}$, while $\Sigma^{-(\alpha=0)}$ will have a constant distribution throughout the disc. The total mass of the cryobelt is set to 60 $M_\oplus$. The mass is subdivided into a number of

small bodies, N, between 125 and 1000. The accuracy of the simulations by Eriksson et. al. (2018) show only marginal improvement when increasing the number of belt particles from 1000 up to 10000.

To illustrate the effects of dynamical friction the planet is included as a massive, $10M_{\oplus}$, planet in MERCURY6's big body input. As the setup is simulating a scattering from the giant planet region, the planet is given an initial eccentricity of 0.95 and 5° of inclination. The semi-major axis, a_{pl}, is varied across experiments; if not specified otherwise, it is set to 600 AU. The other orbital elements are set to 0. The axially symmetric nature of the cryobelt, combined with the comparatively long period of the effects studied, makes the initial values of ω, Ω and ν unimportant.

3.3 Frictionless dynamics

To understand the trajectories of the planet in the argument of periapsis-eccentricity phase space, further simulations were performed. They were constructed to eliminate the effects of dynamical friction by reducing the mass of the planet to be equal to that of bodies in the cryobelt. The cryobelt was still modelled as massive superparticles, identical to the ones in the dynamical friction simulations. This change reduces the rate of dynamical friction, which scales with the mass of the body moving through the medium, but keeps the secular effects from gravitational interactions with the belt.

All the frictionless dynamics simulations were done with a 1000 body cryobelt and with planets with a semi-major axis of 600 AU. The planets were initialised with different values of e and i, set to keep the Kozai parameter at a fixed value. ω was varied in intervals of 90° to explore multiple regions of phase space. Multiple simulations were combined to construct empirical phase portraits for different values of the Kozai parameter. For simulations where a close encounter with a superparticle had impacted the value of the Kozai parameter noticeably, the initial conditions for the cryobelt particles were re-randomised.

3.4 Miyamoto–Nagai potential integration

For the integrations carried out with the Miyamoto–Nagai potential, I implemented the forces in equation 2.7 into the optional user defined force subroutine in MERCURY6 to mimic the cryobelt, previously simulated by superparticles. As the small body input in MERCURY6 was no longer used for simulating the cryobelt, multiple planets with different orbital characteristics were simulated simultaneously as small bodies. This was made possible due to small bodies not interacting with each other. However, it requires all planets in these simulations to have zero mass, otherwise the planets could be perturbed by shifts in the Sun's position caused by the other planets. The other orbital parameters of the planets were retained from the frictionless dynamics simulations.

As MERCURY6's built-in system for calculating energy conservation does not work when a user defined force is included, the energy conservation was checked manually.

A potential issue with the Miyamoto–Nagai potential is that it can not model the gap in the cryobelt between the inner edge and the Sun. The mass enclosed within this region is comparatively small, totalling less than 5% for values of the a parameter higher than 300 AU. The effect of this discrepancy was judged to be small enough that it was outweighed by the benefits of the Miyamoto–Nagai potentials analytical volume density and easily derived forces. For $a = 100$ AU the case where the enclosed mass is significant, 29%, no notable differences were observed compared to the other cases.

Chapter 4

Results

4.1 Dynamical friction simulations

In total, 15 simulations were carried out to investigate dynamical friction. The parameters of all of the simulations are presented in table 4.1, with the accompanying ω-e phase space plots in appendix A. For several of the simulations the parameters were kept the same, with the only change being the disc particles, which were randomly generated for each simulation. The Kozai parameter is not kept at a constant value for these simulations, as dynamical friction and belt interactions will change both the eccentricity and the inclination.

Table 4.1: Table of the parameters for the dynamical friction simulations.

Simulation	$\Sigma^{-\alpha}$	a_{pl}[AU]	N_{bodies}	Time [Gyr]
A_1	1	600	1000	1.00
A_2	1	600	1000	1.00
A_3	1	600	1000	1.00
A_4	1	600	1000	0.85
B_1	0	600	1000	0.80
B_2	0	600	1000	0.75
C_1	1	150	1000	0.20
D_1	1	200	1000	0.30
E_1	1	300	1000	0.40
F_1	1	600	125	1.00
F_2	1	600	125	4.00
F_3	1	600	125	3.00
G_1	1	600	250	3.00
H_1	1	600	500	1.00
H_2	1	600	500	3.00

The examples presented in this section are: simulation A_1 with $a_{pl} = 600$ AU, $N = 1000$ and $\alpha = 1$; simulation B_1 with $a_{pl} = 600$ AU, $N = 1000$ and $\alpha = 0$; and simulation F_2 with $a_{pl} = 600$ AU, $N = 125$ and $\alpha = 1$.

In figure 4.1 two plots from the A_1, B_1 and F_2 simulations are shown: the ω-e phase space, in which we search for indications of libration, to make comparisons with the classical Kozai–Lidov resonance; and the time evolution of the inclination, the predictions of Planet Nine's inclination, presented in Batygin and Brown's review (2019), have been marked in green.

Simulation A_1 starts of on a circulating trajectory, the eccentricity appears to slowly be dampened by dynamical friction. The trajectory exhibits some downwards, step-like, turns. After this, the trajectory librates around 0° and briefly 180°. The planets inclination is initially dampened before it increases sharply at 200 Myr. It reaches a maximum of 39° while ω oscillates around 0°.

Simulation B_1 shows a step-like behaviour similar to simulation A_1, after the eccentricity has been slightly dampened by dynamical friction. The main point of libration is 270°. The inclination is again initially dampened, before a more incremental increase occurs. The planets inclination does not reach values matching Batygin and Brown's prediction until after 500 Myr. The planet reaches a maximum inclination of 35°.

The trajectories of simulations A_1 and B_1 in the ω-e phase space are discussed in more detail in section 4.3.

Simulation F_2 shows a longer evolution than the other simulations at 4 Gyr. After an initial phase of being on a circulating trajectory and slowly dampening eccentricity due to dynamical friction, the eccentricity starts to drop in a step-like behaviour like simulations A_1 and B_1. After approximately 500 Myr the trajectory starts librating around $\omega = 180°$. During the following 3.5 Gyr the trajectory alternately librates around the 0° and 180° islands. The libration is ended by the dynamical friction reducing the eccentricity, and thus increasing the Kozai constant, enough for the fixed points to ceases to exist. The trajectory, now circularised into an orbit with $e \approx 0.2$, performs a series of loops which do not correspond to previous points of libration. During its trajectory simulation F_2 reaches a maximum inclination of 38° while transitioning between fixed points, and periodically reaches similar inclinations while its trajectory is in an island. After circularisation the inclination has reached a value below 5°.

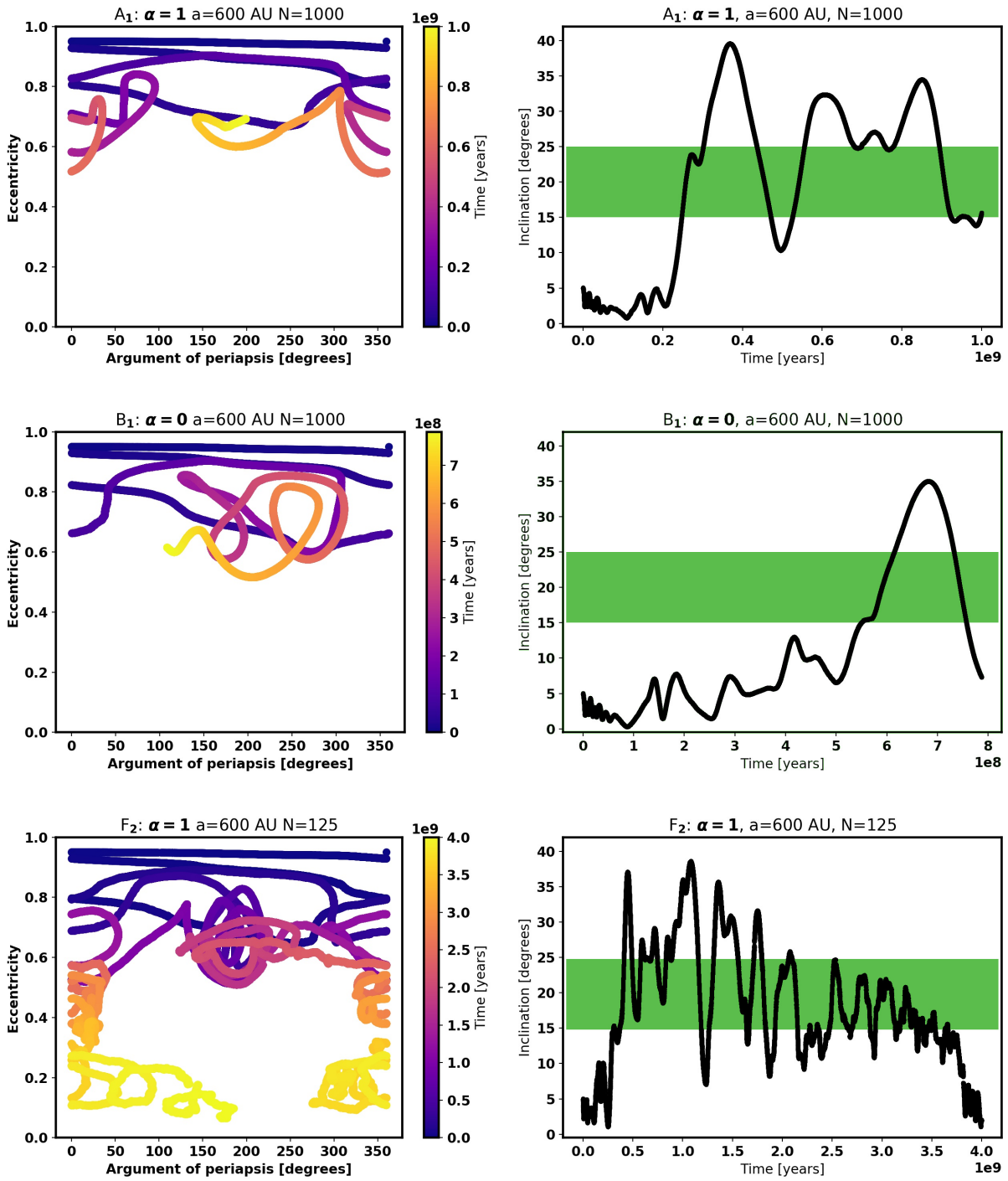

Figure 4.1: Examples of dynamical friction simulations. The eccentricity - argument of periapsis phase space is shown to the left, the colour scale shows time. The time evolution of the inclination is shown to the right, the green area marks the range of inclinations Planet Nine is predicted to have (Brown 2019). Note that the simulations have not run for the same amount of time.

Some general results drawn from the dynamical friction simulations:

- In all simulations the eccentricity of the planet is dampened and the pericenter detaches from Neptune.
- For most simulations the inclination rises sharply while ω oscillates around a fixed value, the exception being the simulations with a reduced semi-major axis.
- In the majority of the simulations, the planets trajectory exhibited an oscillating behaviour around 0° or 180°. In some cases a transition occurred such that the planet changed which angle it librated about.
- For all simulations the Kozai parameter starts at $c = 0.3$. The value of the constant oscillates, generally increasing while passing under fixed points and decreasing while passing over them.
- In simulation F_1, seen in appendix A, the planet ejected 98% of the 125 cryobelt objects, ending the interactions.

4.2 Empirical phase portraits

The empirical phase portraits were constructed to better understand the trajectories in the dynamical friction simulations. Each empirical phase portrait is a combination of a number of individual simulations. The parameters for the empirical phase portraits are shown in table 4.2. The semi-major axis was set to 600 AU and the number of belt particles was 1000. For a surface density distribution with $\alpha = 1$, three phase portraits with different Kozai parameters were constructed, to help with understanding the A_{1-4} simulations. One phase portrait was made with $\alpha = 0$ to help understand simulations B_{1-2}. The Kozai parameter for the simulations is mostly preserved, the largest difference in the Kozai parameter value is $\Delta c = 0.0146$.

All phase portraits show centres around 0° and 180° which are not present in the classical Kozai cycle shown in figure 2.4. The phase portraits showed a lowering of some of their fixed points as the value of the Kozai parameter increases, and a symmetry around 180°, both results similar to the ones in figure 2.4. At 90° and 270°, for low eccentricities, there are fixed points in the empirical phase portraits which most closely resemble the classical Kozai fixed points when it comes to location and the shape of the phase space around them. However, these points rise in eccentricity as the Kozai parameter increases, in contrast to the classical Kozai fixed points in figure 2.4.

The evolution of the trajectories near the saddles was generally slower, leading to more time for random walk to disrupt the trajectory. The saddles are therefore not always clearly visible in the figures, necessitating their inference from the more readily visible centres.

Table 4.2: Table of the simulations performed to get the empirical phase portraits.

$\Sigma^{-\alpha}$	a_{pl}[AU]	N_{bodies}	c	e_{max}	Number of simulations
1	600	1000	0.50	0.87	80
1	600	1000	0.67	0.74	56
1	600	1000	0.75	0.66	44
0	600	1000	0.67	0.74	38

In the empirical phase portraits, figs. 4.2 to 4.5, certain trajectories have been highlighted: the red trajectories are located at high eccentricity, around the 0° or 180° fixed points which have been marked [**a**]; the purple trajectories are located at high eccentricity, around the 90° or 270° fixed points which have been marked [**b**]; the green trajectories are located at low eccentricities, around around the 90° or 270° fixed points which have been marked [**c**]; the blue trajectories are circulating. The maximum allowed eccentricity for each value of the Kozai parameter is displayed with a shaded grey area. All the marked fixed points are centres, between each centre there appears to be a saddle.

- The phase portrait in figure 4.2 for $c = 0.50$ has [**a**] and [**b**] centres, and what appears to be either [**c**] centres which have not yet been found, or a region where [**c**] centres will appear for a slightly higher value of the Kozai parameter. The [**b**] centres appear to be a bit higher in eccentricity than the [**a**] ones.

- In the phase portrait in figure 4.3 for $c = 0.67$, the [**b**] centres present in figure 4.2 appear to have disappeared, leaving a pair of saddles between the two [**a**] centres. What was just a hint of [**c**] centres for $c = 0.50$, have now appeared at $e = 0.2$.

- In the phase portrait in figure 4.4 for $c = 0.75$, the [**b**] centres are now more clearly gone. The size of the islands have increased markedly, leaving only a thin band of circulating trajectories. The eccentricity of the [**c**] centres continues to rise up to $e = 0.27$.

- The phase portrait in figure 4.5 for $c = 0.67$ and $\alpha = 0$ has prominent [**b**] centres, differentiating the simulation from figure 4.3 with the same Kozai parameter. The additional fixed points makes the phase portrait more similar in appearance to figure 4.2, with the notable exception of the maximum eccentricity being lower and the presence of the [**c**] centres.

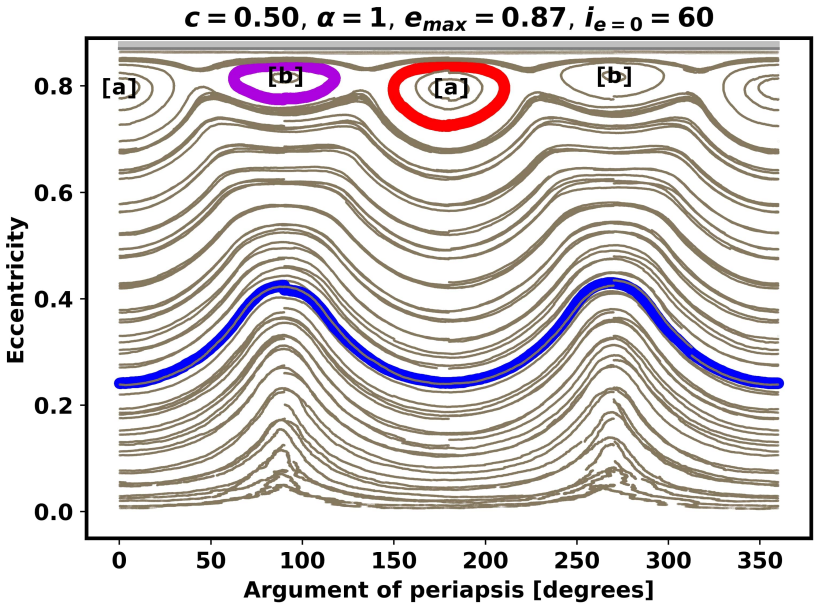

Figure 4.2: Empirical phase portrait for c=0.50. Examples of librating trajectories in red and purple, circulating trajectory in blue.

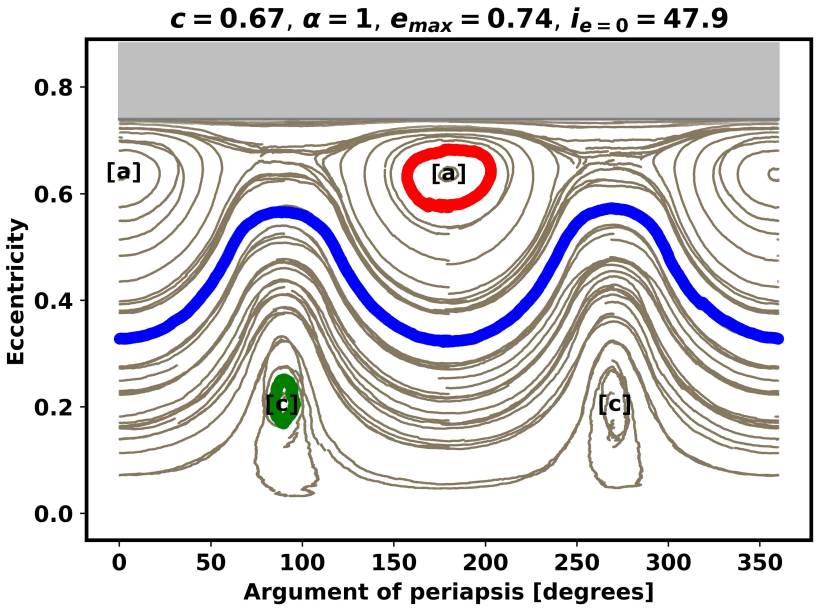

Figure 4.3: Empirical phase portrait for c=0.67. Examples of librating trajectories in red and green, circulating trajectory in blue.

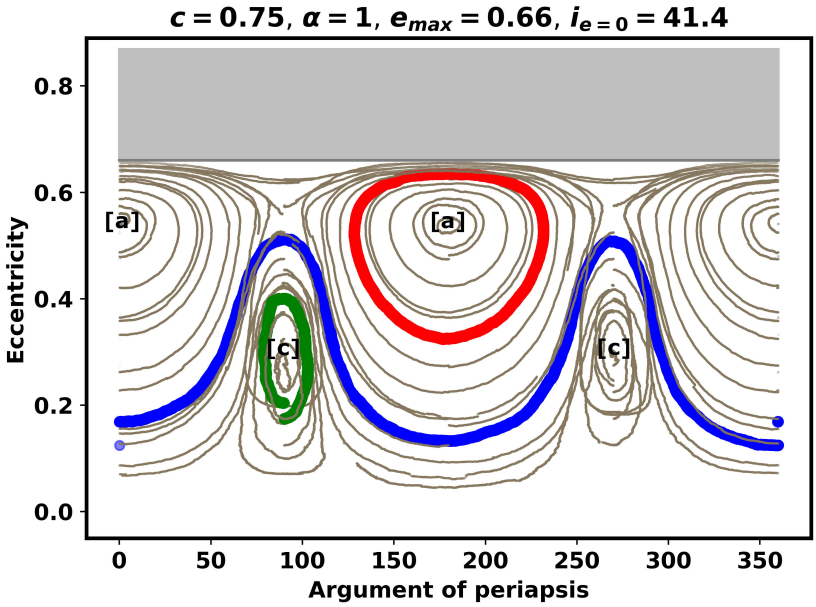

Figure 4.4: Empirical phase portrait for c=0.75. Examples of librating trajectories in red and green, circulating trajectory in blue.

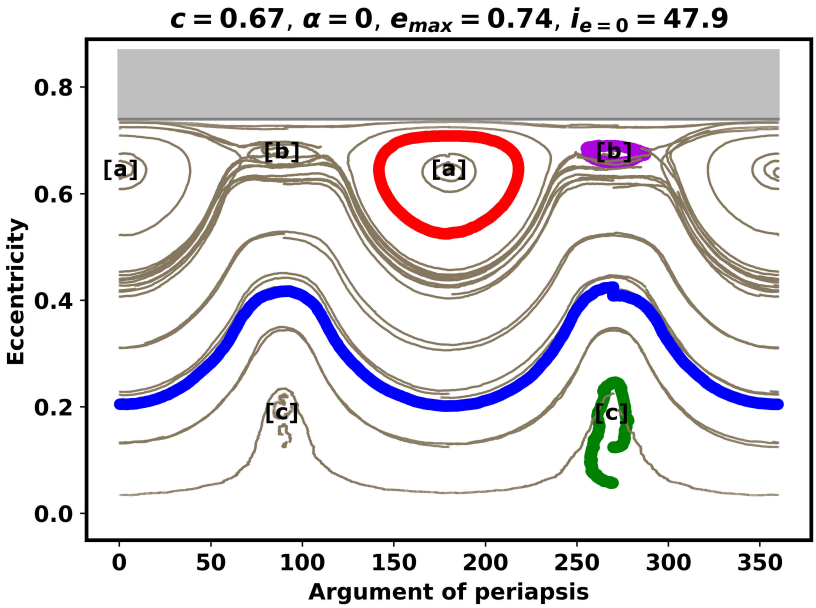

Figure 4.5: Empirical phase portrait for c=0.67 with a constant surface density distribution. Examples of librating trajectories in red, purple and green, circulating trajectory in blue.

4.3 Simulation trajectories

On their own, the causes of the twists and turns in the trajectories in the dynamical friction simulations, figure 4.1, appear opaque. In this section the trajectories have been plotted together with the empirical phase portraits to better understand those causes, and a tentative explanation for what happens is presented.

4.3.1 Trajectory of simulation $\mathbf{A}_1$

Figure 4.6 shows simulation A_1 overlaid on the three empirical phase portraits, with the colour scale representing time. A separate illustration of the trajectory, colour coded with the value of the Kozai parameter, is also presented. In that plot, red rectangles highlight three key features, which are further elaborated on in the list below. Beneath the trajectories is a plot of the Kozai parameter over time, which gives additional information for what causes the twists and turns, the key regions have been highlighted here as well. The different centres will be referred to as **[a]**, **[b]** and **[c]**, as shown in figs. 4.2 to 4.5.

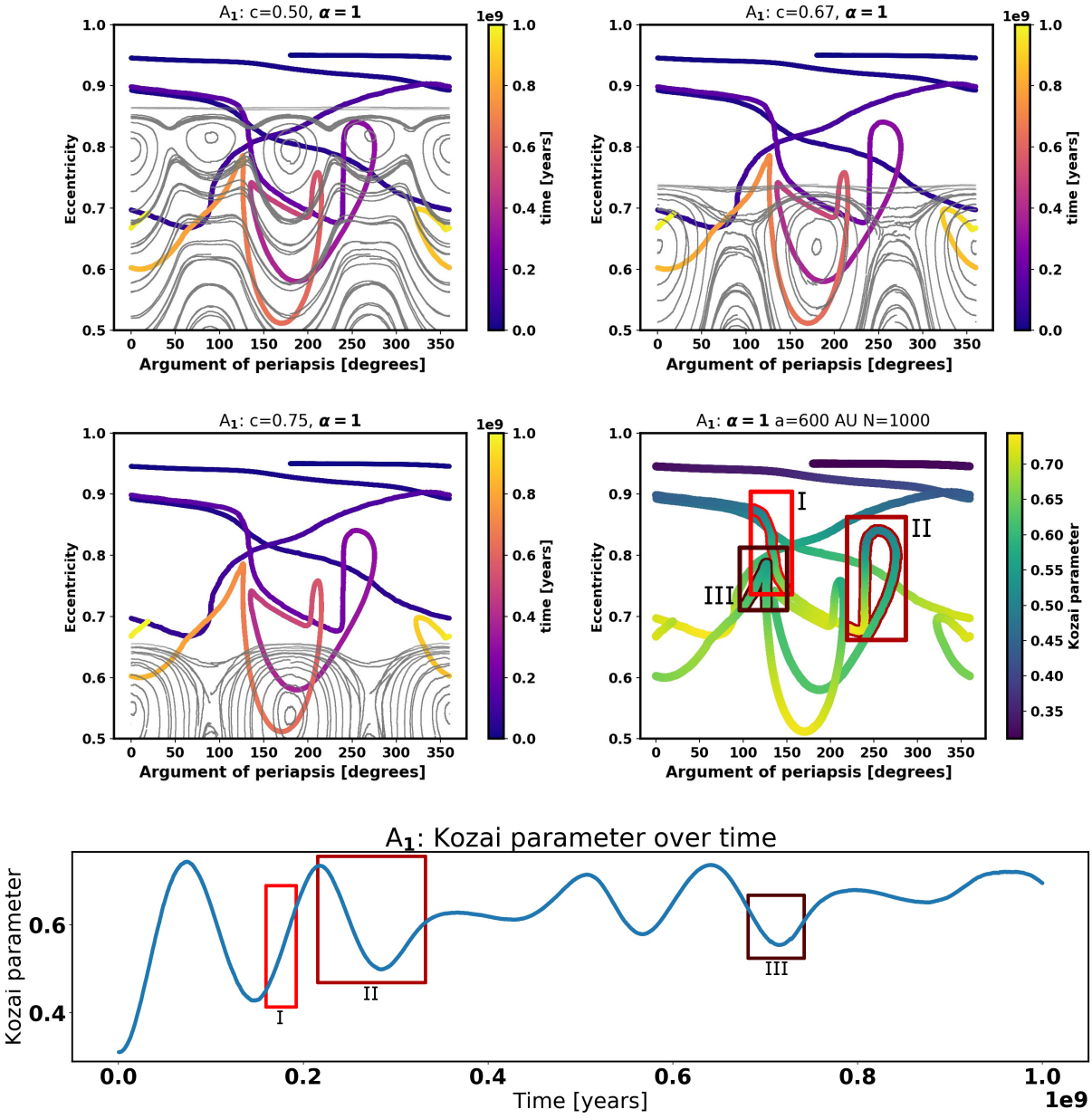

Figure 4.6: The trajectory of simulation A_1 from the dynamical friction simulations has been overlaid on the empirical phase portraits for $c = 0.50, 0.67, 0.75$, with $\alpha = 1$. The values of ω for simulation A_1 have been shifted 180°, to centre the main point of libration. The fourth panel has a different colour scale to show what value the Kozai parameter has at different points of the trajectory. Three key features of interest have been highlighted and are further elaborated on in section 4.3.1. To further clarify how the Kozai parameter changes, its time evolution has been added below thew four panels, with the key regions highlighted as well.

I The first region features a downwards turn, levelling out at the end. In section 4.1 this feature is referred to as step-like.

The top left phase portrait best reflects the start of the trajectory as it passes above the [**b**] centre. As the trajectory gets close to the saddle point between the [**b**] and [**a**] centres, the colour scale in the fourth frame and the plot of the Kozai parameter over time show that the Kozai parameter starts to steadily increase as the trajectory starts to bend downwards. The trajectory is stuck at this saddle throughout the decrease in eccentricity. The end state of the trajectory in this region, above the [**a**] centre at 180°, is best seen in the top right phase portrait.

The cause of the trajectories downwards turn is the increasing Kozai parameter and the resulting fall in eccentricity for the fixed points. In this region the trajectory does not pass below the fixed points.

II The second region features the trajectory doing an almost closed, stretched out, loop.

The top right phase portrait best shows the start of the trajectory, as it has hit the saddle between the two [**a**] centres. As the Kozai parameter steadily sinks, as we can see in the bottom plot, the trajectory goes straight up. At the top, the trajectory is better seen in the top left phase portrait. The Kozai parameter has decreased enough that the [**b**] centre has appeared and the trajectory starts to pass above it. As it does, we can see in the bottom plot that the Kozai parameter starts to rise again. This causes the [**b**] centre to disappear, and the trajectory bends back towards the [**a**] centre, passing below it.

The decreasing Kozai parameter causes the upward turn at the start of the region. But, the main thing shaping the trajectory is the appearance and disappearance of the [**b**] centre. In this region the trajectory passes from above to below the fixed points.

III The third region features the trajectory doing a more than 270° turn.

The top left phase portrait best shows the entirety of the trajectory. Hitting the saddle between [**a**] and [**b**] centres, the trajectory is sharply turned away, passing below the [**b**] centre. The Kozai parameter is seen to first decrease slightly before rising an equal amount.

The main thing shaping this part of the trajectory is the shape of the phase portrait. The circulating trajectories in the top right empirical phase portrait also feature sharp turns at the saddles. This effect is then amplified by the change in the Kozai parameter switching signs.

By looking closer at these key features we can see the competing effects of dynamical friction described in section 2.3. Changing the Kozai parameter will both move the position of the fixed point and cause them to appear and disappear, affecting the trajectory. Dynamical friction will cause the dampening of the eccentricity seen initially. After the initial dampening, the effects of dynamical friction still occur, but become harder to spot, as something causes the Kozai parameter to periodically decrease.

4.3.2 Trajectory of simulation B_1

Figure 4.7 shows a similar setup as figure 4.6, but as there is only one available empirical phase portrait, a thorough analysis of every turn can not be performed, as it is unknown how the fixed points evolve under a changing Kozai parameter. However, some general observation can be made about the differences between the two sets of simulations. The [**b**] centres, which are present at $c = 0.67$ for this empirical phase portrait, but missing from the ones for $\alpha = 1$ in figure 4.3, appear to be the main points of libration for simulation B_1. Step-like shapes, where the trajectory bends over the fixed points as the Kozai parameter changes, are present in both simulations, but are more pronounced in simulation B_1, possibly because of the increased number of fixed points in the empirical phase portrait. A loop-like shape is present at approximately 130°, possibly indicating the presence of additional fixed points beyond the ones in figure 4.5.

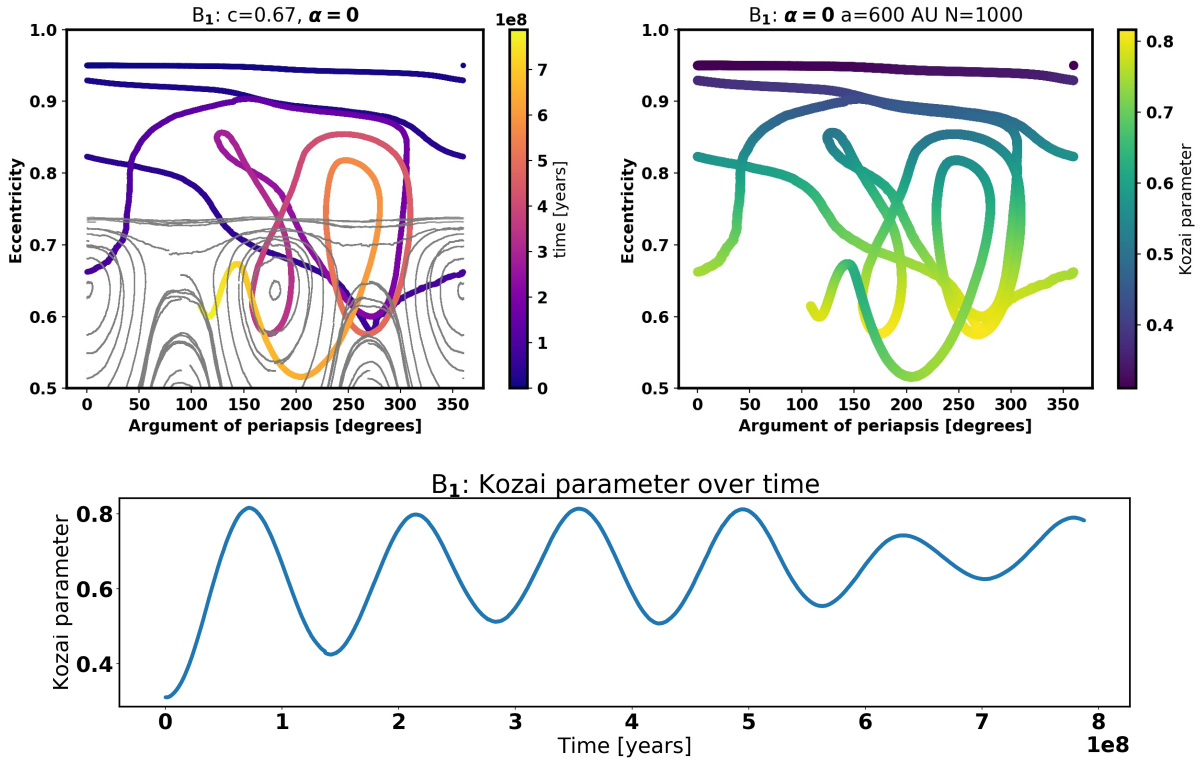

Figure 4.7: Evolution of simulation B_1 overlaid on the empirical phase portrait for $c = 0.67$, $\alpha = 1$

4.4 Miyamoto–Nagai phase portraits

24 simulations were performed with the Miyamoto–Nagai potential. The same values of the Kozai parameter were investigated as in the empirical phase portraits. For each value

of the Kozai parameter four different values of the disc parameter a were tested, and two different values of disc parameter b.

The computational time required to produce a phase portrait with the Miyamoto–Nagai potential is approximately 100 times shorter than the time required to produce an empirical phase portrait. The value of the Kozai parameter was preserved to a notably higher rate than in the frictionless dynamics simulations, with the maximum Δc being on the order of 10^{-4}.

For all simulations two centres were found at $\omega = 90°$ and $270°$. The size of the islands would increase with increasing a. Increasing b had a negligible effect for the simulations with $a > 300$ AU. For the simulations with $a = 100$ AU, increasing b lifted the fixed points noticeably, as the oblateness of the disc was significantly decreased.

In figure 4.8, $c = 0.75$, $a = 1500$ AU and $b = 50$ AU. Approximately 7% of the mass is within the planets semi-major axis of 600 AU. The phase portrait bears a strong resemblance to the ones in figure 2.4 for the classical Kozai cycle where the perturber was exterior to the planet.

In figure 4.9, $c = 0.50$, $a = 300$ AU and $b = 10$ AU. Approximately 55% of the mass is within the planet's semi-major axis of 600 AU. The lowering of the Kozai parameter has lowered the fixed points compared to figure 4.8. The decrease in the a parameter has reduced the size of the island of librating trajectories around the fixed point. There is now quite clearly saddle points present between the centres.

The phase portraits obtained have several major differences from the empirical phase portraits. At a minimum, two centres are missing; no centres appeared at $\omega = 0°$ or $180°$ in any of the simulations with the Miyamoto–Nagai potential. Unlike the [**c**] centres, the centres in these simulations will drop in eccentricity as the Kozai parameter increases, in line with the regular Kozai cycle.

Manually checking the fractional energy change for these simulations shows that the simulations are conserving energy well. The largest error was $\frac{dE}{E} = 0.0015$ for $c = 0.50$, $a = 100$, $b = 10$. Simulations with a higher value for a showed $\frac{dE}{E}$ values an order of magnitude smaller.

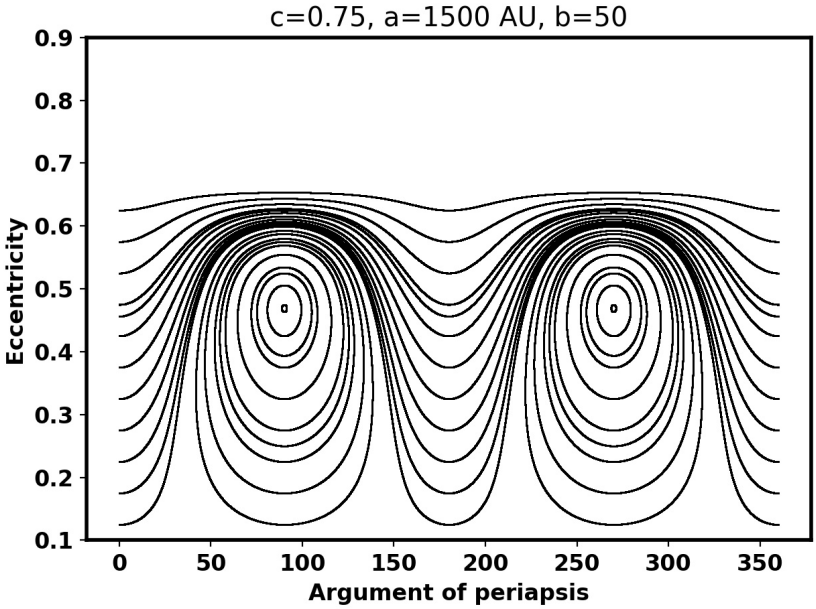

Figure 4.8: Phase portrait where the Miyamoto–Nagai potential mimics the cryobelt.

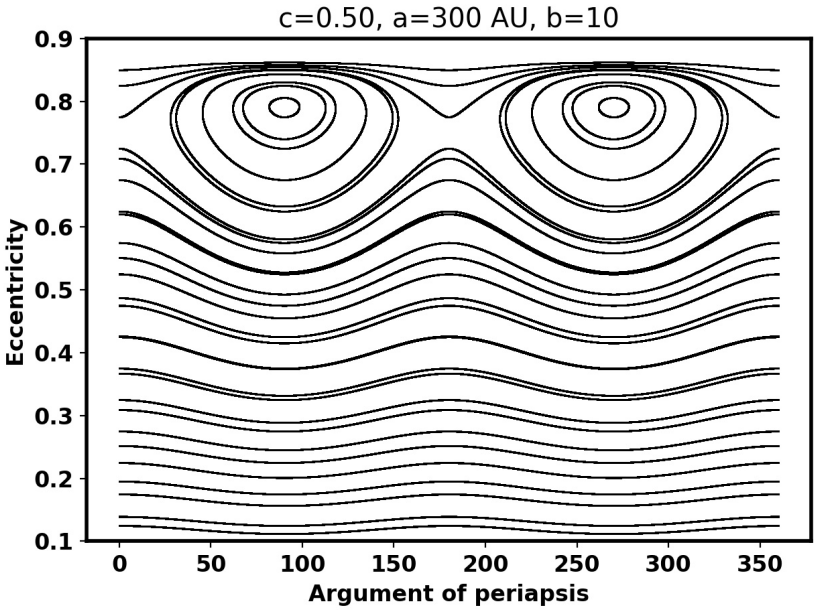

Figure 4.9: Phase portrait where the Miyamoto–Nagai potential mimics the cryobelt.

Chapter 5

Discussion and conclusions

5.1 Initial goals and future possibilities

The initial goal of this project was to find a way to investigate the competing effects of dynamical friction and the Kozai–Lidov resonance on a planet traversing a planetesimal disc, and to find when these effects led to an excitation of the orbits inclination. This would be accomplished by using the dynamical friction equations with some volume density representing the cryobelt, and to combine those equations with the classical Kozai equations of motion. Since the discovery of the additional fixed points, the focus shifted to mapping out the phase portraits for the system.

For a more complete understanding of the possible orbital characteristics of Planet Nine, or any other high eccentricity planet interacting with a planetesimal disc, several steps could be taken.

- Producing more empirical phase portraits for a wider range of values of the Kozai parameter could aid understanding of how the fixed points in these portraits move, appear and disappear.

- Repeating this process for other values of the disc parameters, surface density distribution and disc mass among other possibilities, could assist in narrowing down what factors are important for the planet-belt dynamics.

- Finding a potential/density pair which aids computational time and eliminates potentially unphysical effects from interactions with superparticles would be very valuable, both for quicker production of phase portraits, but also for combination with the dynamical friction equations.

- The cause of the changing value of the Kozai parameter could be another topic of further research. Dynamical friction is expected to drive the Kozai parameter up by lowering eccentricity, but at certain times it is seen to fall, as seen in section 4.3.1. The feedback on the disc could be a potential cause of this and an area for further research.

- Comparisons between this work and that of Thomas and Morbidelli (1996) on the topic of long-period comets could be made, as their comets are getting trapped in a Kozai–Lidov resonance with an interior perturber, showing similarities to the setup considered for this thesis.

5.2 Conclusions

- In the simulations performed in this project, planets moving through an extended disc of planetesimals will reliably be circularised by the dynamical friction, in line with the findings of Eriksson et. al. (2018).

- The inclination of the planets in the simulations is reliably excited to levels close to the ones predicted by the simulations of Batygin and Brown (2019).

- The planets argument of periapsis is seen to oscillate around fixed values in combination with an exchange of eccentricity and inclination. This is in line with the classical Kozai–Lidov resonance, but the ω-e phase portrait for the system shows that there are significant differences. The most important of these differences is the presence of fixed points at high eccentricities and multiples of 90° in argument of periapsis.

- Of the additional fixed points found in the phase portraits, the ones at 0° and 180° appear to play the most important role for the later evolution of the planet, being the main points of libration.

- Mimicking the cryobelt with the Miyamoto–Nagai potential will yield computation times which are lower by two orders of magnitude, but will not give analogous results, due to differences in the phase portraits. Adjusting the disc parameters of the potential will change the shape of the phase portrait as the mass distribution changes, but it has failed to produce additional fixed points.

Bibliography

Batygin, Konstantin and Michael E. Brown (2016). "Evidence for a Distant Giant Planet in the Solar System". In: *AJ* 151, 22, p. 22. DOI: 10.3847/0004-6256/151/2/22. arXiv: 1601.05438 [astro-ph.EP].

Batygin, Konstantin, Michael E. Brown, and Hayden Betts (2012). "Instability-driven Dynamical Evolution Model of a Primordially Five-planet Outer Solar System". In: *ApJ* 744.1, L3, p. L3. DOI: 10.1088/2041-8205/744/1/L3. arXiv: 1111.3682 [astro-ph.EP].

Binney, James and Scott Tremaine (2008). *Galactic dynamics.* Princeton series in astrophysics. Princeton University Press. ISBN: 9780691130262. URL: http://ludwig.lub.lu.se/login?url=http://search.ebscohost.com.ludwig.lub.lu.se/login.aspx?direct=true&db=cat07147a&AN=lub.1799576&site=eds-live&scope=site.

Brown, Michael E. (2019). "The Planet Nine hypothesis". In: *Physics Today* 72.3, pp. 70–71. DOI: 10.1063/PT.3.4172.

Carrera, Daniel et al. (2017). "Planetesimal Formation by the Streaming Instability in a Photoevaporating Disk". In: *ApJ* 839, 16, p. 16. DOI: 10.3847/1538-4357/aa6932. arXiv: 1703.07895 [astro-ph.EP].

Chambers, J. E. (1999). "A hybrid symplectic integrator that permits close encounters between massive bodies". In: *MNRAS* 304, pp. 793–799. DOI: 10.1046/j.1365-8711.1999.02379.x.

Del Popolo, A., E. Spedicato, and M. Gambera (1999). "Kuiper Belt evolution due to dynamical friction". In: *A&A* 350, pp. 685–693. arXiv: astro-ph/9905014 [astro-ph].

Eriksson, Linn E. J., Alexander J. Mustill, and Anders Johansen (2018). "Circularizing Planet Nine through dynamical friction with an extended, cold planetesimal belt". In: *MNRAS* 475, pp. 4609–4616. DOI: 10.1093/mnras/sty111. arXiv: 1710.08295 [astro-ph.EP].

Goldstein, Herbert, Charles P. Poole, and John Safko (2014). *Classical mechanics.* Pearson. ISBN: 9781292026558. URL: http://ludwig.lub.lu.se/login?url=http://search.ebscohost.com.ludwig.lub.lu.se/login.aspx?direct=true&db=cat07147a&AN=lub.4569375&site=eds-live&scope=site.

Kenyon, Scott J. and Benjamin C. Bromley (2016). "Making Planet Nine: Pebble Accretion at 250-750 AU in a Gravitationally Unstable Ring". In: *ApJ* 825.1, 33, p. 33. DOI: 10.3847/0004-637X/825/1/33. arXiv: 1603.08008 [astro-ph.EP].

Kokubo, E. and S. Ida (1995). "Orbital evolution of protoplanets embedded in a swarm of planetesimals." In: *Icarus* 114.2, pp. 247–257. DOI: 10.1006/icar.1995.1059.

Kozai, Yoshihide (1962). "Secular perturbations of asteroids with high inclination and eccentricity". In: *AJ* 67, p. 591. DOI: 10.1086/108790.

Li, Gongjie and Fred C. Adams (2016). "Interaction Cross Sections and Survival Rates for Proposed Solar System Member Planet Nine". In: *ApJ* 823.1, L3, p. L3. DOI: 10.3847/2041-8205/823/1/L3. arXiv: 1602.08496 [astro-ph.EP].

Lidov, M. L. (1962). "The evolution of orbits of artificial satellites of planets under the action of gravitational perturbations of external bodies". In: *Planetary and Space Science* 9, pp. 719–759. DOI: 10.1016/0032-0633(62)90129-0.

Miyamoto, M. and R. Nagai (1975). "Three-dimensional models for the distribution of mass in galaxies." In: 27, pp. 533–543.

Mustill, Alexander J., Sean N. Raymond, and Melvyn B. Davies (2016). "Is there an exoplanet in the Solar system?" In: *MNRAS* 460, pp. L109–L113. DOI: 10.1093/mnrasl/slw075. arXiv: 1603.07247 [astro-ph.EP].

Nesvorný, David and Alessandro Morbidelli (2012). "Statistical Study of the Early Solar System's Instability with Four, Five, and Six Giant Planets". In: *AJ* 144.4, 117, p. 117. DOI: 10.1088/0004-6256/144/4/117. arXiv: 1208.2957 [astro-ph.EP].

Press, William H. et al. (2007). *Numerical recipes : the art of scientific computing.* Cambridge University Press. ISBN: 9780521880688.

Thomas, Fabrice and Alessandro Morbidelli (1996). "The Kozai Resonance in the Outer Solar System and the Dynamics of Long-Period Comets". In: *Celestial Mechanics and Dynamical Astronomy* 64.3, pp. 209–229. DOI: 10.1007/BF00728348.

Trujillo, Chadwick A. and Scott S. Sheppard (2014). "A Sedna-like body with a perihelion of 80 astronomical units". In: *Nature* 507, pp. 471–474. DOI: 10.1038/nature13156.

Valtonen, Mauri J. and Hannu Karttunen (2006). *The three-body problem.* Cambridge : Cambridge University Press, 2006. ISBN: 9780521852241.

Wikipedia, the free encyclopedia (2007). *Orbital elements.* [Online; accessed June 08, 2019]. URL: https://en.wikipedia.org/wiki/Orbital_elements#/media/File:Orbit1.svg.

Appendix A

Dynamical friction simulations

For all simulations $e_{planet} = 0.95$, $i_{planet} = 5^{\circ}$, $M_{planet} = 3E-05\ M_{\odot}$, $R_{in} = 100$ AU, $R_{out} = 600$ AU, $M_{belt} = 60 M_{\oplus}$.

Table A.1: Table of the parameters for the dynamical friction simulations.

Simulation	$\Sigma^{-\alpha}$	a_{pl}[AU]	N_{bodies}	Time [Gyr]
A_1	1	600	1000	1.00
A_2	1	600	1000	1.00
A_3	1	600	1000	1.00
A_4	1	600	1000	0.85
B_1	0	600	1000	0.80
B_2	0	600	1000	0.75
C_1	1	150	1000	0.20
D_1	1	200	1000	0.30
E_1	1	300	1000	0.40
F_1	1	600	125	1.00
F_2	1	600	125	4.00
F_3	1	600	125	3.00
G_1	1	600	250	3.00
H_1	1	600	500	1.00
H_2	1	600	500	3.00

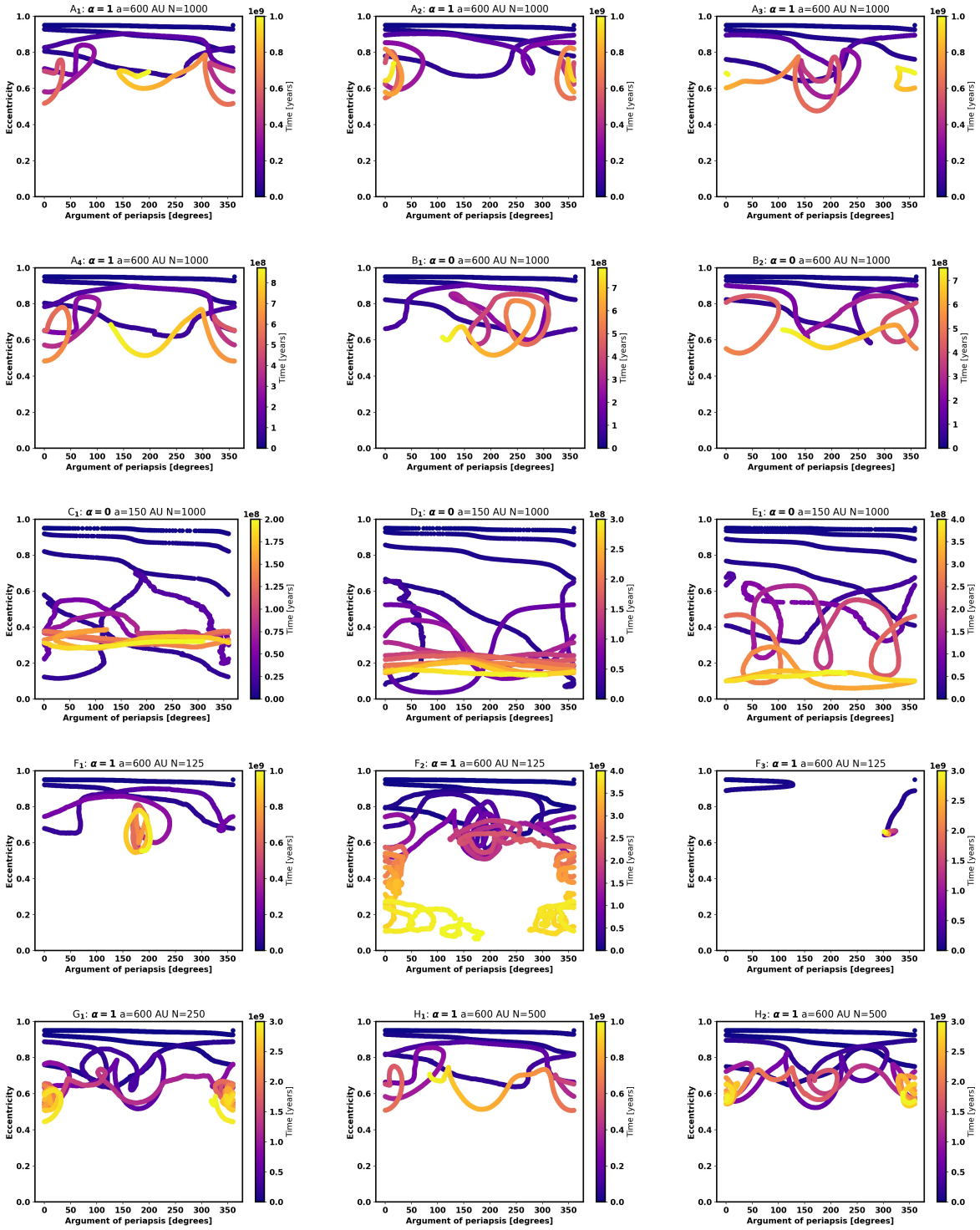

Figure A.1: Dynamical friction plots, parameters of which are found in table 4.1.

Appendix B

Miyamoto–Nagai phase portraits

The images are organised with each Kozai parameter having its own page, a increasing downwards and b increasing left to right. All parameters shown in table B.1.

Table B.1: Table of the simulations performed to get the empirical phase portraits.

c	a[AU]	b[AU]
0.50	100	10
0.50	100	50
0.50	300	10
0.50	300	50
0.50	600	10
0.50	600	50
0.50	1500	10
0.50	1500	50
0.67	100	10
0.67	100	50
0.67	300	10
0.67	300	50
0.67	600	10
0.67	600	50
0.67	1500	10
0.67	1500	50
0.75	100	10
0.75	100	50
0.75	300	10
0.75	300	50
0.75	600	10
0.75	600	50
0.75	1500	10
0.75	1500	50

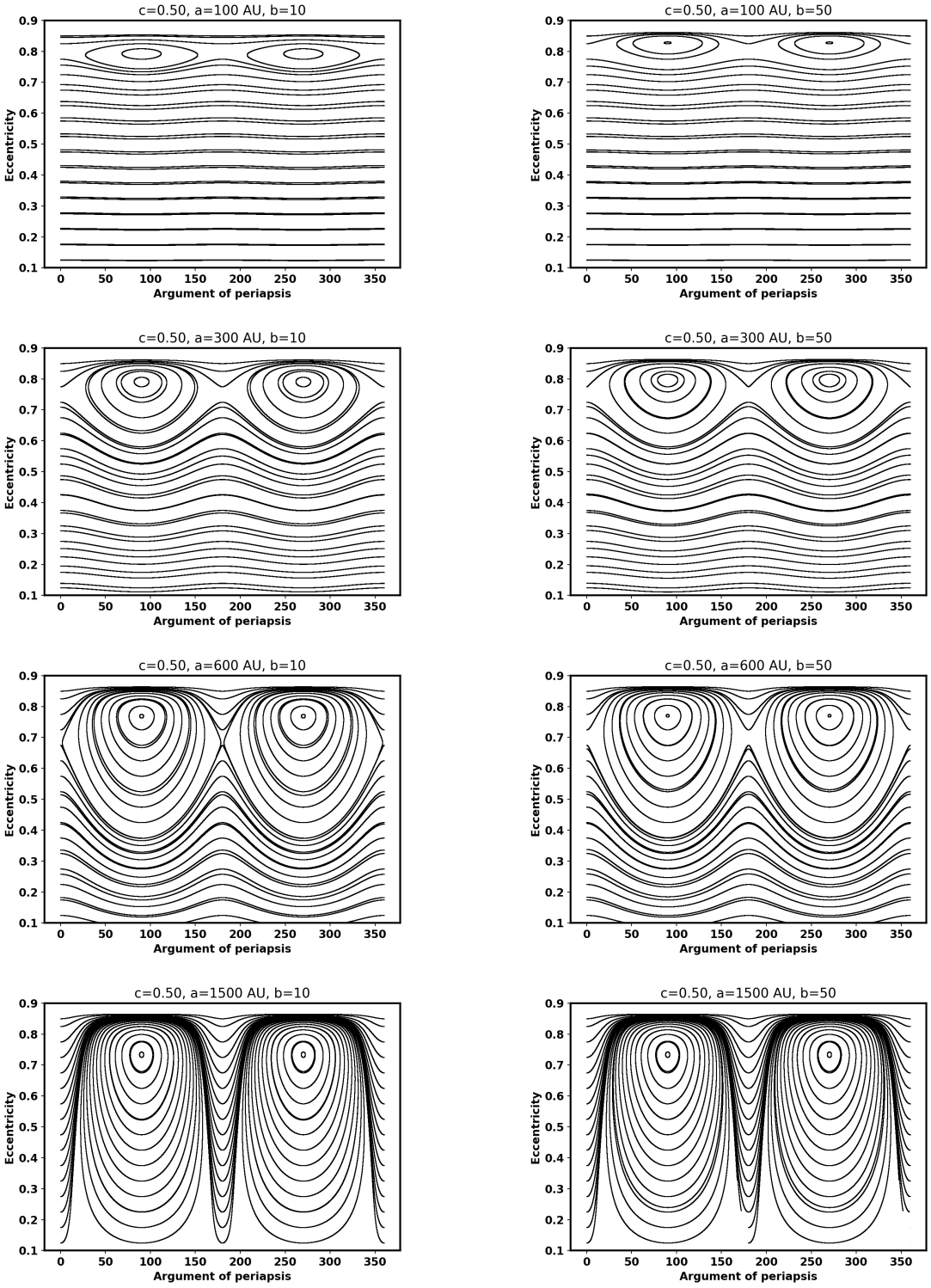

Figure B.1: Phase portraits with the Miyamoto–Nagai potential. The Kozai parameter is 0.50 for all plots. The y-scale displays eccentricity between 0.1 and 0.9.

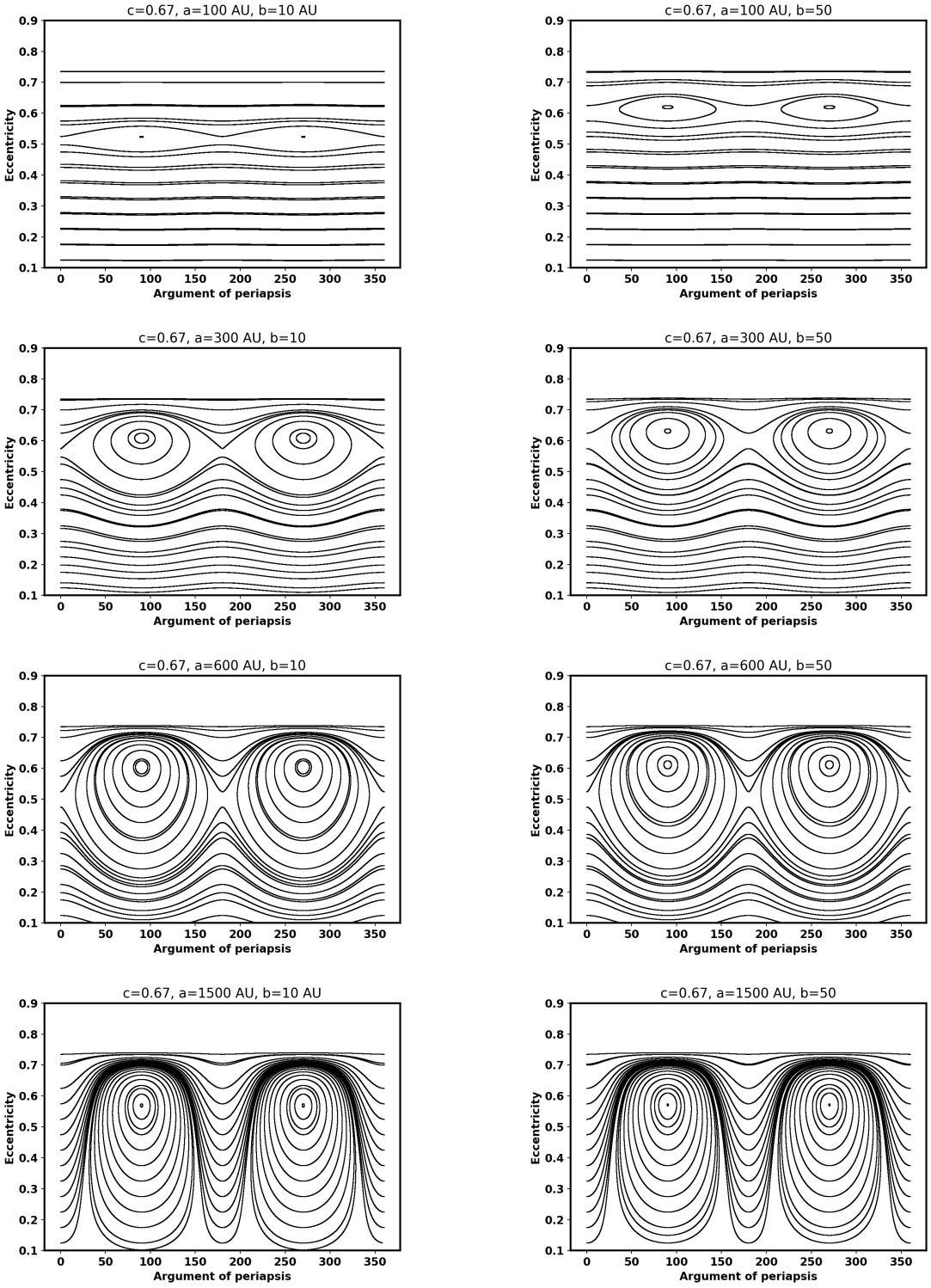

Figure B.2: Phase portraits with the Miyamoto–Nagai potential. The Kozai parameter is 0.67 for all plots. The y-scale displays eccentricity between 0.1 and 0.9.

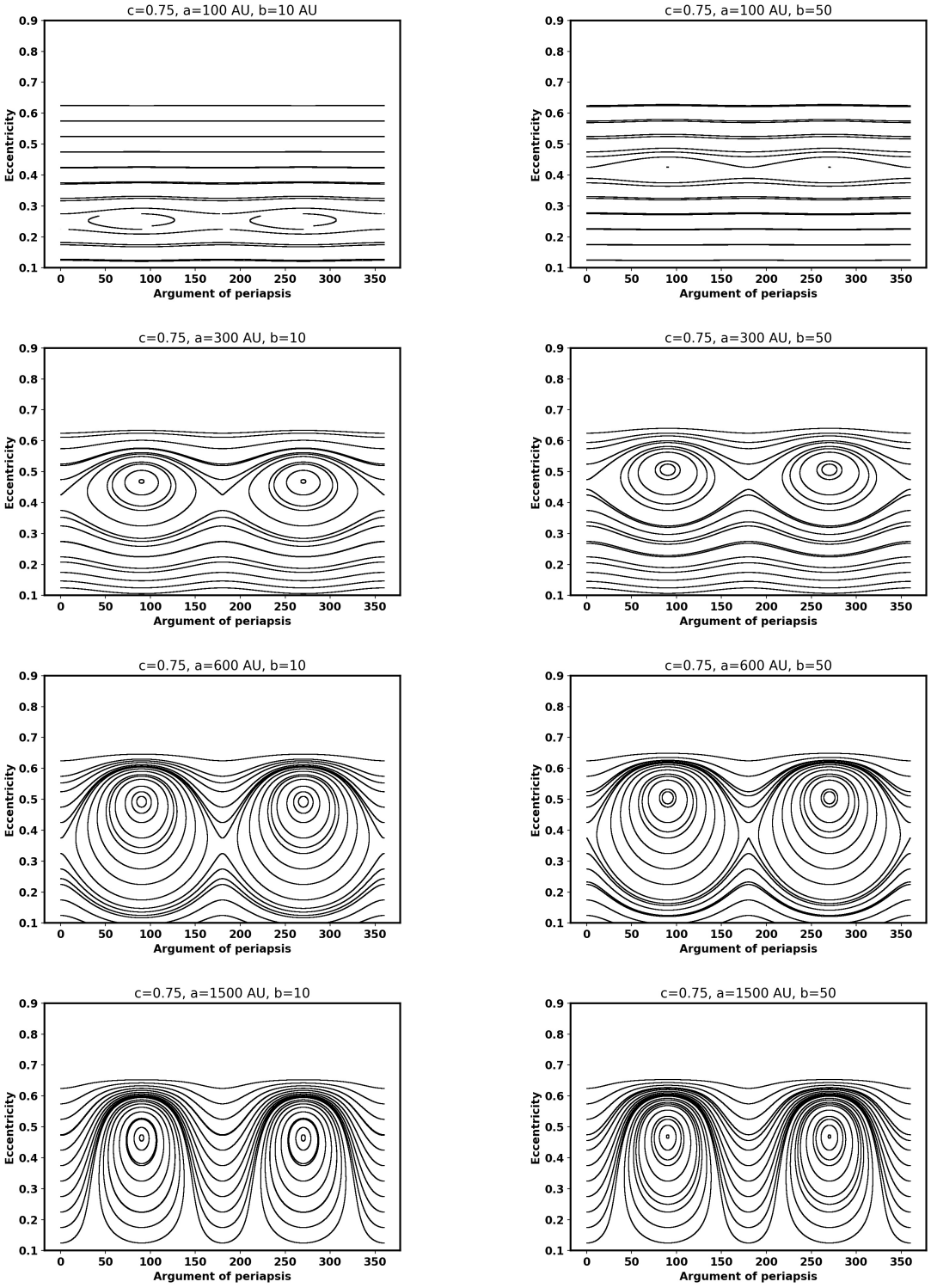

Figure B.3: Phase portraits with the Miyamoto–Nagai potential. The Kozai parameter is 0.75 for all plots. The y-scale displays eccentricity between 0.1 and 0.9.